

Density Functional Theory Analysis of Hexagonal Close-Packed Elemental Metal Photocathodes

Tuo Li,^{1,*} B. L. Rickman,¹ and W. Andreas Schroeder¹

¹*Department of Physics, University of Illinois at Chicago,
845 W. Taylor Street, Chicago, Illinois 60607-7059, USA*

(Dated: March 20, 2015)

A density function theory (DFT) based analysis of photoemission from hexagonal close packed (hcp) metals is presented and the calculated values of the rms transverse momentum (Δp_T) are in good agreement with the available experimental data on Be and Mg [*Phys. Rev. Lett.*, 111:237401, (2013); *Proceedings of LINAC 2002*, Gyeongju, Korea, (2002)]. The lattice constants and work functions of the hcp metals are also examined and are consistent with the available experimental values. In addition, emission from (0001)-oriented Be is examined due to the presence of a strong surface state.

PACS numbers: TBA

Keywords: Photocathodes, DFT Calculations, HCP Metals, Photoemission, Surface States

I. INTRODUCTION

The performance of Ultrafast Electron Microscopy (UEM) [1, 2], Dynamic Transmission Electron Microscopy (DTEM) [3–6], Free Electron Lasers (FELs) and X-Ray Free Electron Lasers (XFELs) is fundamentally dependent upon the quality in the transverse direction of the electron pulses produced by their front-end laser-driven electron gun. In the transverse spatial dimension, a high quality (high brightness) electron pulse requires a low normalized spatial transverse rms emittance; commonly defined as $\varepsilon_T = \Delta x \Delta p_T / m_0 c$, where Δx is the rms transverse pulse size, Δp_T is the rms transverse momentum of the electrons in the pulse, m_0 is the free electron mass, and the c is the speed of light in vacuum. In propagation through perfect (i.e., non-aberrating) electron optics and the transverse emittance of the electron pulse is conserved [7], which generally implies that its initial value at the photocathode must be minimized to obtain a high brightness electron source. The initial electron beam size is limited by either (i) laser beam focusing constraints (i.e., physical optics), (ii) laser-induced optical damage of the photocathode surface, or (iii) screening of the photo-guns accelerating field near the photocathode surface [8–11] that causes temporal [12] and spatial [13] electron pulse distortion. It is therefore likely that any major improvements in the performance of research instruments employing pulsed laser-driven electron sources will require a significant reduction in the rms transverse momentum Δp_T of the front-end electron source.

Prior theoretical analyses [14, 15] have provided an expression for the rms transverse momentum for planar metal photocathodes; $\Delta p_T = \sqrt{m_0(\hbar\omega - \phi)/3}$, where ϕ is the effective work function (including the Schottky effect [16]) and $\hbar\omega$ is the incident photon energy. However, these analyses have assumed a perfect canonical metal —

one with isotropic parabolic bands (i.e., a single spherical Fermi surface) and positive dispersions associated with the free electron mass m_0 . Such an approximation for the electronic band structure of metal photocathodes is unrealistic for all but a few elemental metals, perhaps the body-centered cubic Group I alkali metals and the face-centered cubic Group Ib noble metals. Most elemental metals are known to have anisotropic Fermi surfaces due to either the energetic position of the Fermi level in the electronic band structure or the intrinsic anisotropy of the metal's crystalline structure. The latter is the subject of this paper; specifically, the hexagonal close-packed (hcp) structure [17–29] which is the most prevalent crystal space group amongst the elemental metals. Further complicating a theoretical evaluation of the rms transverse momentum is the known strong work function anisotropy in hcp metals [30–32]. As a result, both the excess photoemission energy and the electronic band structure, which together determine the states that may contribute to emission, are dependent on the $(ijkl)$ emission direction, and hence, so will be Δp_T . In fact, one should also expect the transverse momentum distribution of the emitted electrons to be spatially anisotropic for certain orientations of the uniaxial hcp crystals.

In this work, we describe a density functional theory (DFT) approach to determining the rms transverse momentum Δp_T of electrons emitted from hcp elemental metals. Section II outlines the first principles methods, compares the obtained lattice constant ratios with known experimental values, and presents the results of a thin-slab method [33] to evaluate the work function $\phi_{(ijkl)}$. In Section III, we reduce the 15 possible hcp elemental metal photocathodes to four, based on a set of reasonable selection criteria. The DFT-based photoemission analysis is then described in Section IV, using emission from the (0001) face of Mg as an example. Thereafter, emission from the most prevalent face of hcp metals is simulated for Be, Mg, Y, and Zr, and the theoretical values of Δp_T are compared to available experimental data for polycrystalline Be [34] and Mg [35] photocathodes. Finally,

* tli27@uic.edu

in Section VI, an analysis of Be(0001) photocathodes is presented where a robust surface state [36, 37] can contribute to photoemission.

II. FIRST-PRINCIPLES METHODS: BULK PROPERTIES, BAND STRUCTURE, AND WORK FUNCTION

Any rigorous theoretical analysis of photoemission from a crystalline material requires a knowledge of the band structure near the Fermi level; in particular, the precise energy-momentum relationships, $E(\vec{k})$, of the occupied states and their associated local density of states, $g(E, \vec{k})$. In addition, knowledge of the photoelectric work function, $\phi_{(ijkl)}$, in the $(ijkl)$ crystalline direction of photoemission from hexagonal close-packed (hcp) crystals is required in order to determine which occupied states may contribute to the emission. In sections IV and V below, we present the results of such a photoemission analysis, directed to the evaluation of Δp_T , for a selected set of hcp metals (Section III). In this section, we describe the first-principles methods employed to determine the electronic band structure of hcp metals and their orientation dependent work function, both of which are dependent upon accurate values of the a and c hcp lattice constants. The results are compared, therefore, to measured lattice constants and, for the latter, to both experimental and theoretical literature values of $\phi_{(ijkl)}$.

The first step in a first-principles photoemission analysis of hcp metals is an evaluation of their electronic band structure. These calculations within DFT employ the PWscf code of the Quantum-ESPRESSO suite [38]. Ultrasoft pseudopotentials (USPP) within the local density approximation (LDA) [39] are used for all 15 hcp metals; the results of our analysis are not changed if the generalized gradient approximation (GGA) [40] is used instead. A Monkhorst-Pack [41] set of special k -points and Marzari-Vanderbilt smearing [42] with a broadening of 0.02 Ryd is employed and, for the $4d$, $5d$ and $6p$ metals, relativistic approximations are included [43, 44]. In addition, ferromagnetic collinear local spin density approximation (LSDA) has been performed to find the optimized geometry of hcp Co due to its magnetic property [45]. The DFT-based calculations were all initiated using the experimental lattice parameters for each hcp metal and then tested for total energy convergence to a tolerance of 10^{-4} eV using a uniform grid of k -points. Minimization of the total energy then yields the theoretical optimized lattice constants a and c that are compared in Table I to their experimental values.

The comparison of the DFT-generated lattice constants with the experimental values in Table I not only shows good agreement, but also reveals a wide range in the c/a lattice constant ratio from 1.567 for Be to 1.886 for Cd. This ratio range is related to electronic state mixing and hence anisotropy in the electronic band structure. In the divalent hcp metals Be, Mg, Zn, and Cd

TABLE I. Calculated lattice constants of the 15 hcp metals compared with the experimental literature results.

	Expt. (a.u.)	Expt. c/a	DFT (a.u.)	DFT c/a
Be	$a=4.32$	1.567 [46]	$a=4.20$	1.590
	$c=6.77$		$c=6.68$	
Cd	$a=5.63$	1.886 [17]	$a=5.48$	1.896
	$c=10.62$		$c=10.39$	
Co	$a=4.74$	1.571 [28]	$a=4.52$	1.617
	$c=7.45$		$c=7.31$	
Hf	$a=6.04$	1.579 [43]	$a=5.88$	1.594
	$c=9.54$		$c=9.37$	
Mg	$a=6.06$	1.625 [47]	$a=5.89$	1.642
	$c=9.85$		$c=9.67$	
Os	$a=5.17$	1.579 [43]	$a=5.17$	1.571
	$c=8.16$		$c=8.12$	
Re	$a=5.22$	1.609 [48]	$a=5.04$	1.587
	$c=8.40$		$c=8.00$	
Ru	$a=5.10$	1.582 [43]	$a=5.16$	1.663
	$c=8.07$		$c=8.58$	
Sc	$a=6.24$	1.591 [49]	$a=6.03$	1.589
	$c=9.93$		$c=9.52$	
Tc	$a=5.18$	1.585 [30]	$a=5.11$	1.624
	$c=8.21$		$c=8.30$	
Tl	$a=6.53$	1.599 [29]	$a=6.40$	1.608
	$c=10.44$		$c=10.29$	
Ti	$a=5.58$	1.586 [49]	$a=5.36$	1.612
	$c=8.85$		$c=8.64$	
Y	$a=6.89$	1.572 [49]	$a=6.61$	1.587
	$c=10.83$		$c=10.49$	
Zn	$a=5.01$	1.804 [17]	$a=4.83$	1.888
	$c=9.04$		$c=9.12$	
Zr	$a=6.10$	1.595 [43]	$a=5.91$	1.636
	$c=9.73$		$c=9.67$	

the p valence electron levels are closest to the occupied s levels whereas electrons in the d levels are energetically well separated from both in Zn and Cd. As a consequence, in Be and Mg, high-symmetry $s-p$ mixing is linked to a preferred formation of the energy band near the Fermi level, and thus, electronic band structures with close to parabolic dispersion below the Fermi level. However, there is no similarity between the alkali metal's close to spherical Fermi surfaces and those of Be and Mg [50] due to the latter's non-cubic crystal symmetry and the fact that two valence electrons ensure that their Fermi surfaces enclose twice the volume in momentum space. Nonetheless, Mg with a c/a lattice constant ratio of 1.624 is within 1% of ideal close packing where $c/a = 1.633$. In contrast, for Cd and Zn there is a significant mixing contribution from the d states which leads to large non-ideal c/a ratios of 1.886 and 1.896, respectively. For Tl, the only $6p$ hcp transition metal, $c/a = 1.599$; its Fermi surface consists of three non-spherical structures [51] and its

Fermi energy lies in an almost pure $6p$ band above the top of the s band. According to the extensive investigations by F. Batallan et al. [28], R.A. Deegan [52], and D.G. Pettifor [53], the electronic bands of the other ten d -block transition metals ($3d$ (Co, Sc and Ti), $4d$ (Ru, Tc, Zr and Y) and $5d$ (Hf, Re and Os)) are primarily d -like and not parabolic near Fermi level. They have low lying d levels leading to a s - p and d synthesized band structures with the c/a ratios from 1.540 to 1.609. The large variation in the c/a lattice constant ratios and associated electronic band structure details for the hcp elemental metals generates anisotropic Fermi surfaces and energy-momentum relationships $E(\vec{k})$, and thus asymmetric local densities of states $g(E, \vec{k})$, in addition to considerable work function anisotropy, $\phi_{(ijkl)}$ — all of which are involved in photoemission for any particular crystal direction.

Knowledge of the photoelectric work function and its anisotropy is the second requirement for our DFT-based photoemission analysis. We evaluate $\phi_{(ijkl)}$ using the thin-slab method [54] which requires knowledge of the atomic potentials, their lattice positions in the ABAB z -direction hexagonal stacking (Table I), and the metal's Fermi level acquired from the bulk DFT band structure calculations. Unrelaxed slabs generally consisting of 8-13 atomic layers separated by a 15 Å vacuum region are employed as this is sufficient to ensure that both the vacuum and average crystal potential reach equilibrium. The work function may then be determined from the energetic difference between the Fermi and the vacuum levels to a calculation uncertainty of typically ± 0.05 eV. Even though the LDA can be expected to represent the better choice of exchange-correlation functional if a better match to experimental values of $\phi_{(ijkl)}$ is desired, the surfaces of the hcp metals are known to be less likely to reconstruct at low temperatures, so that even with surface relaxations, neither the LDA nor the GGA exchange-correlation functional appear to represent a more accurate choice [55]. Our evaluated results for the work functions of the (0001) and (10\bar{1}0) crystal faces for all 15 hcp elemental metals are shown in Table II, together with available experimental and theoretical values from the literature. The tabulated data clearly shows that the intrinsic anisotropic nature of hcp metals also results in a strong crystal orientation dependence of the work function.

III. PHOTOCATHODE SELECTION CRITERIA

Although, in principle, all 15 elemental hcp metals could be employed as photocathodes given the appropriate UV laser radiation source (i.e., incident photo energy), differences in their physical and chemical characteristics will dictate their utility. Ideally, a photocathode material should possess a work function that allows photoemission with readily available UV laser sources, be robust and chemically stable, have a sufficiently high melting point, and be free of magnetic effects.

TABLE II. Work functions of the 15 hcp metals

	Surface	ϕ (eV)	Method	ϕ_{DFT} (eV)
Be	(P) ^a	3.92 [56]	Expt.	
	(P)	4.98 [57]	Expt.	
	(0001)	5.10 [27]	Expt.	5.61
		5.40 [58]	Theory	
		5.62 [24]	Theory	
	(10\bar{1}0)			3.88
Cd	(P)	4.22 [57]	Expt.	
	(0001)	4.00 [59]	Expt.	4.17
	(10\bar{1}0)			4.76
Co	(P)	5.00 [57]	Expt.	
	(0001)	5.55 [60]	Expt.	5.62
Hf	(P)	3.90 [57]	Expt.	
	(0001)			4.51
	(10\bar{1}0)			3.63
Mg	(P)	3.66 [57]	Expt.	
	(0001)	4.05 [21]	Theory	3.87
		3.70 [58]	Expt.	
	(10\bar{1}0)			3.79
Os	(P)	4.83 [57]	Expt.	
	(0001)			5.62
	(10\bar{1}0)			4.94
Re	(P)	4.96 [57]	Expt.	
	(0001)	5.22-5.77 [61]	Expt.	5.35
	(10\bar{1}0)	5.75 [57]	Expt.	5.67
Ru	(P)	4.71 [57]	Expt.	
	(0001)	5.40 [62]	Expt.	5.37
	(10\bar{1}0)			4.59
Sc	(P)	3.50 [57]	Expt.	
	(0001)			3.81
	(10\bar{1}0)			3.10
Tc	(P)	4.88 [57]	Expt.	
	(0001)			5.15
	(10\bar{1}0)			4.31
Tl	(P)	3.84 [57]	Expt.	
	(0001)			3.90
	(10\bar{1}0)			3.93
Ti	(P)	4.33 [57]	Expt.	
	(0001)	4.60(± 0.2) [63]	Expt.	4.72
	(10\bar{1}0)			3.63
Y	(P)	3.10 [57]	Expt.	
	(0001)			3.60
	(10\bar{1}0)			3.08
Zn	(P)	4.33 [57]	Expt.	
	(0001)	4.15 [21]	Theory	4.43
	(10\bar{1}0)			5.04
Zr	(P)	4.05 [57]	Expt.	
	(0001)	4.26-4.51 [64]	Theory	4.42
	(10\bar{1}0)			3.59

(P)=Polycrystalline

1. *Work function.* Although modern laser systems are capable of generating radiation throughout most of the infrared, visible, and ultraviolet (UV) spectral regions, the most readily accessible wavelengths are the harmonics of solid-state lasers such as Ti:sapphire (emitting at ca. 800nm), Nd:YAG (1064nm), and Yb:fiber based systems (\sim 1040nm). As the efficient generation of harmonics shorter than \sim 250nm is complicated by the availability of suitable UV transparent nonlinear crystals, desired photocathodes have work functions less than $\hbar\omega \approx 4.7$ eV (i.e., the third harmonic of Ti:sapphire or the fourth harmonic of Nd:YAG). From Table II, one can see that this tends to rule out Co, Os, Re, and possibly Ru and Tc — elements that also have availability issues.

2. *Robustness and chemical stability.* The metal photocathode should also be hard enough to allow for a good surface figure to be attained by polishing (to avoid surface roughness effects [65]) and ideally be sufficiently inert chemically to allow for operation at vacuum pressures greater than 10^{-9} Torr (as routinely found in electron microscopes). The former criterion rules out thallium, which is an extremely soft metal, while the latter suggests that Hf, Ti, and Sc photocathodes are likely to be problematic as they oxidize immediately upon exposure to air. In general, of course, one expects the work function, and hence electron emission, to be altered upon surface oxidation [66].

3. *Melting point and optical damage.* Metal photocathodes with melting points above \sim 1,000K are also preferred for short electron pulse generation as laser induced heating [67, 68] can be significant. Cadmium and zinc, which have melting points below 600K, do not meet such a requirement. Of course, this form of optical damage may be preceded by other forms of laser radiation induced damage that are generally dependent upon the optical surface quality of the photocathode.

4. *Magnetism.* Magnetic metals such as Co, and the face-centered cubic metals Ni and Fe, do not generally perform well as low emittance photocathode materials, primarily because the trajectory of photoemitted electrons is strongly affected by the metals' local surface magnetic field [69].

Based on these selection criteria, we will restrict our analysis of the photoemission characteristics of elemental hcp metal photocathodes to Be, Mg, Y, and Zr. The fact that the hcp crystal structure is intrinsically anisotropic, and hence, so is the electronic crystal band structure, immediately suggests that the momentum distribution of electrons photoemitted from the (0001) crystal face should be different to that emitted from the (10 $\bar{1}$ 0) face. As shown in Sections IV and V below, this is indeed the case even after accounting for the difference in work function for the two faces (Table II). In general, it is only photoemission from the (0001) face that may generate an electron beam with an isotropic transverse momentum distribution. Consequently, the emission characteristics of Mg(0001) will first be used to introduce our DFT-based photoemission model.

IV. DFT BASED PHOTOEMISSION MODEL AND Δp_T ANALYSIS

From a knowledge of the band structure of the metal photocathode (i.e., the electronic state dispersion $E(\vec{k})$ and local density of states $g(E, \vec{k})$) and the work function anisotropy ϕ_{ijkl} , it is straightforward to determine the momentum components of the photoemitted electron and the weighted (by $g(E, \vec{k})$) probability of its emission from a particular crystal face over the work function barrier, $T(\vec{p}, \vec{p}_0)$, where $p_0 = \hbar k_0$ is the momentum of the emitted electron in the vacuum. As the momentum of the incident UV photon is negligible in comparison to the momentum of the electron in the crystal ($\hbar k \gg \hbar\omega/c$) [34], the governing energy-momentum relationship for an instantaneous (one-step) photoemission process involving a virtual optically-excited state is

$$\hbar\omega + E(p_z, p_T) = \phi_{ijkl} + \frac{1}{2m_0}(p_{z0}^2 + p_T^2), \quad (1)$$

where the Fermi level is defined as zero energy. In Equation (1), the electron momentum is written in terms of its longitudinal component $p_z = \hbar k_z$ ($p_{z0} = \hbar k_{z0}$) perpendicular to the ($ijkl$) emission surface in the metal (vacuum), and its transverse component $p_T = \hbar k_T$ parallel to the surface which is conserved during the emission process [7]. The flux transmission probability over the work function barrier may be expressed as

$$T = \frac{m_z^*}{m_0} \frac{4p_z p_{z0}}{(p_z + p_{z0})^2}; \quad \frac{1}{m_z^*} = \left| \frac{\partial^2 E}{\partial p_z^2} \right|, \quad (2)$$

where the magnitude of the local effective mass in the emission direction, m_z^* , is used to account for both electron-like (positive dispersion) and hole-like (negative dispersion) of the emitting band(s). The close relationship between the band dispersion $E(\hbar\vec{k} = \vec{p}_z + \vec{p}_T)$ below the Fermi level in the photocathode material and the photoemitted electron momentum distribution is clearly evident in Equations (1) and (2). In particular, if the band dispersion restricts electrons with high values of p_T from being emitted (an imaginary p_{z0}), then a reduced value of the emitted rms transverse momentum Δp_T should result. Figure 1 displays the DFT based photoemission simulation results for emission from the (0001) face of magnesium ($\phi_{(0001)} = 3.87(\pm 0.05)$ eV). Fig. 1(a) illustrates the electronic states that contribute to the photoemission (shaded region) below the Fermi level (solid line) along two crystal momentum directions (10 $\bar{1}$ 0) and (01 $\bar{1}$ 0) transverse to the (0001) emission direction when the incident photon energy is 4.75 eV; that is, for an excess energy $\Delta E = 0.88(\pm 0.05)$ eV. As expected from the band structure calculations [47, 70], the emission states in the basal plane of this hcp metal are electron-like (positive dispersion) and highly symmetric about the (0001) emission direction for this metal. The dashed line in Fig. 1(a) indicates the maximum possible transverse momentum for the photoemitted electrons, which is simply given

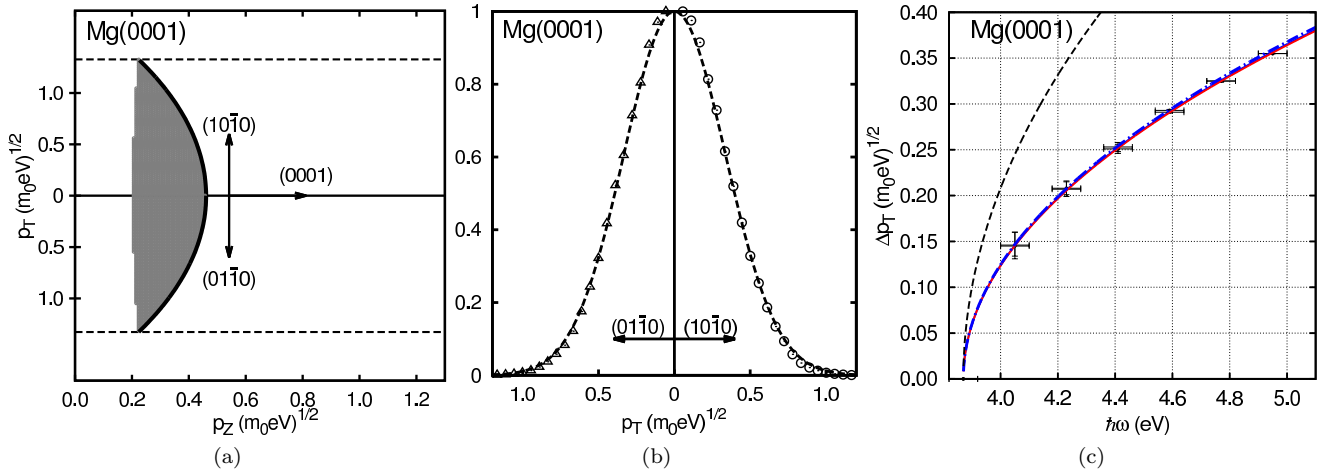


FIG. 1. Mg(0001) photoemission analysis results for $\hbar\omega = 4.75\text{eV}$. (a) Crystal momentum map of the electronic states (shaded regions) below the Fermi level (solid line) that may photoemit within $p_{T,max.} = \sqrt{2m_0\Delta E}$ (dashed lines) for the transverse $(10\bar{1}0)$ and $(01\bar{1}0)$ crystal directions; (b) Transverse momentum distributions of the photoemitted electrons in the $(10\bar{1}0)$ and $(01\bar{1}0)$ directions (Gaussian fits are guides to the eye); (c) Incident photon energy dependence of the rms transverse momentum Δp_T for electron temperatures $T_e \rightarrow 0$ (data points with solid red line fit; $\Delta p_T = A\sqrt{m_0\Delta E}$), $T_e = 300\text{K}$ (dot-dashed line), together with the expected form of $\Delta p_T(\hbar\omega)$ from Refs. [14] and [15] (dashed line).

by $p_{T,max.} = (2m_0\Delta E)^{1/2} \approx 1.327 (m_0\text{eV})^{1/2}$. At this value of the transverse momentum, the transmission efficiency over the photoemission barrier, $T(p_z, p_{z0})$, is zero since $p_{z0} = 0$, so that the transverse momentum distributions of the emitted electrons terminate at $p_{T,max.}$. As the transverse momentum p_T is reduced, more electron states below the Fermi level can contribute to photoemission with those states nearest the Fermi level having the largest local density of states $g(E, \vec{k})$ and the highest values of $T(p_z, p_{z0})$.

The high transverse symmetry of the Γ_4^- emission band about the (0001) crystal direction ensures that the resulting weighted transverse momentum distributions of the photoemitted electrons are nearly identical along the $(10\bar{1}0)$ and $(01\bar{1}0)$ crystal momentum directions (Fig. 1(b)). These p_T distributions for the emitted electrons in the two crystal directions, which are normalized at $p_T = 0$, are generated by summing the product $g(E, \vec{p}_z + \vec{p}_T)T(p_z, p_{z0})$ at discrete values of p_T over the electronic states along p_z that may contribute to photoemission (i.e., solutions to Equation (2) with $p_{z0} > 0$). The spatially-averaged value of the rms transverse momentum Δp_T extracted from these p_T distributions for Mg(0001) emission is $0.322(\pm 0.008) (m_0\text{eV})^{1/2}$ — a value which is only 60% of that predicted by prior analyses [14, 15]; $\Delta p_{T0} = 0.542(\pm 0.015) (m_0\text{eV})^{1/2}$. The explanation for the lower than expected value of Δp_T is associated with the energetic position and dispersion of the Γ_4^- electron band. Our band structure calculations indicate that the energetic minimum of this band at the Γ point is only 1.2 eV below the Fermi level. As a result, for $\Delta E \approx 0.9$ eV, nearly all the available states along the (0001) crystal direction at $p_T = 0$ are accessed, generating a gibbous, rather than crescent, shape to the shaded

region in Fig. 1(a). Thus, disproportionately more states at lower p_T emit than at higher p_T , which yields a reduced value of Δp_T .

Figure 1(c) displays the dependence of Δp_T on the incident photon energy $\hbar\omega$ predicted by the DFT-based simulation for photoemission from Mg(0001). The solid line is a fit to the theoretical data points of the form $\Delta p_T = A\sqrt{m_0(\hbar\omega - \phi_{(0001)})}$, giving a value for A of 0.343. Comparing this value of A with 0.577 from $\Delta p_{T0} = \sqrt{m_0\Delta E/3}$ (dashed line in Fig. 1(c)), again indicates that the rms transverse momentum from Mg(0001) is a factor of ~ 1.7 less than expected from prior analyses [14, 15]. Both of these evaluations of Δp_T are, of course, determined in the ‘zero temperature’ limit; that is, for an electron temperature $T_e \rightarrow 0$, so that no electrons occupy states above the Fermi level. The dot-dashed line (just above the solid line) in Fig. 1(c) shows the predicted form of $\Delta p_T(\hbar\omega)$ when $T_e = 300\text{K}$ (data points not shown) which is evaluated by including the Fermi-Dirac function $f(E) = 1/(1 + \exp[-(E_F - E)/k_B T_e])$, where k_B is Boltzmann’s constant, to describe the occupation of the electronic states around the Fermi energy E_F , albeit for the ‘zero temperature’ crystal band structure. The increase (or change) in Δp_T is less than 1% in this case since ΔE and the value of E_F measured from the bottom of the Γ_4^- band are both much greater than $k_B T_e$; that is to say that the additional partially populated states above the Fermi level are a very small perturbation in the photoemission simulation. Even if T_e is increased to 923K, the theoretical increase in Δp_T is insignificant compared to the uncertainties on the DFT-based photoemission simulation. We note that the Boltzmann tail of the Fermi-Dirac distribution will allow photoemission for

$\hbar\omega < \phi_{(0001)}$ [67], essentially photo-assisted thermionic emission, but this effect is not considered here as the emission efficiency is much reduced.

V. (10 $\bar{1}$ 0)-FACE EMISSION FROM Be, Mg, Y AND Zr

The preferred surface crystal orientation for nearly all hcp polycrystalline metals exposes the (10 $\bar{1}$ 0) face rather than the (0001) face [72]. Accordingly, in this section, we present the results obtained from the DFT-based simulation for photoemission from the (10 $\bar{1}$ 0) crystal face of the selected Be, Mg, Y, and Zr elemental metal photocathodes. The thin-slab analysis [33] indicates that $\phi_{(10\bar{1}0)}$ ranges from 3.08 eV for Y to 3.88 eV for Be (see Table II). As a result, for incident 4.75 eV (or even 4.67 eV) UV photons, one might expect efficient ($\sim 10^{-4}$ [35]) isotropic photoemission since the maximum possible transverse momentum $p_{T,max.} = (2m_0\Delta E)^{1/2}$ of around 1.5 ($m_0\text{eV})^{1/2}$ should allow access to many electronic states in the metal photocathodes. However, as shown below, the highly anisotropic band structure (due to the symmetry of hcp crystals) can play a major role in determining the rms transverse momentum Δp_T of the photoemitted electrons, even generating beams with a highly elliptical divergence symmetry from the (10 $\bar{1}$ 0) face.

Figure 2 displays the results obtained from the DFT-based photoemission simulation for the (10 $\bar{1}$ 0) face of Be, Mg, Y and Zr when $\hbar\omega=4.75$ eV. In each case, Fig. 2(a) shows the electronic states (shaded regions) below the Fermi level (solid line) that contribute to photoemission along the (0001) and (01 $\bar{1}$ 0) crystal momentum directions perpendicular to the (10 $\bar{1}$ 0) emission direction. An acute asymmetry of the contributing states in transverse momentum p_T , caused by the energetic position of the Fermi level in the hcp band structure, is immediately evident, with Be being the most asymmetric and Zr the most symmetric. For Be (10 $\bar{1}$ 0) emission, the hole-like dispersion of the contributing Δ_2 band in the (0001) direction is so strong that emission ceases for $p_T > 0.4$ ($m_0\text{eV})^{1/2}$, even though electron emission up to $p_{T,max.} = 1.319$ ($m_0\text{eV})^{1/2}$ (dashed line) from the same band is possible in the (01 $\bar{1}$ 0) momentum direction. The Δ_2 band also contributes to the state asymmetry for Mg emission although to a somewhat lesser extent as some photoemission is now also possible at $p_{T,max.} = 1.386$ ($m_0\text{eV})^{1/2}$ (dashed line) in the (0001) transverse momentum direction due to the T_2 and T_4 bands [70]. There is also an additional anisotropic contribution to photoemission from Mg from the electron-like Σ_1 band at lower values of p_z . For Y, a large number of predominantly hole-like electronic states, that are more isotropically distributed about the (10 $\bar{1}$ 0) emission direction than in Be and Mg and extend to $p_{T,max.}=1.828$ ($m_0\text{eV})^{1/2}$ (dashed line) in both the transverse (0001) and (01 $\bar{1}$ 0) crystal momentum directions, will contribute to the photoemission. For the

(10 $\bar{1}$ 0) face of Zr, photoemission with $\hbar\omega=4.75$ eV is possible up to $p_{T,max.} = 1.523$ ($m_0\text{eV})^{1/2}$ (dashed line) in all transverse directions and the contributing states appear to be even more symmetrically distributed about the (10 $\bar{1}$ 0) emission direction. The photoemitting states for both Y and Zr are terminated by the MK edge of Brillouin zone at $p_z = 2.93$ ($m_0\text{eV})^{1/2}$ and $p_z = 3.21$ ($m_0\text{eV})^{1/2}$, respectively.

The trend of decreasing anisotropy from Be, through Mg and Y, to Zr is reflected in the transverse momentum distributions of the emitted electrons shown in Fig. 2(b) (center panel). For example, for Be (10 $\bar{1}$ 0) emission at the considered 4.75 eV photon energy, the calculated rms transverse momentum for photoemitted electrons parallel to the (0001) crystal direction, $\Delta p_{T,(0001)} = 0.147$ ($m_0\text{eV})^{1/2}$, is a factor of more than two lower than that for the (01 $\bar{1}$ 0) crystal direction, $\Delta p_{T,(01\bar{1}0)} = 0.312$ ($m_0\text{eV})^{1/2}$. From the summary of the DFT-based evaluations presented in Table III, one sees that this ratio is reduced to ~ 1.4 for Mg emission, and further reduced for Y and Zr emission, respectively, with emission from the latter being close to isotropic. Also listed in Table III is the value of the rms transverse momentum expected from the isotropic single-band theory of Dowell and Jensen [14, 15]; namely, $\Delta p_T = \sqrt{m_0\Delta E/3}$ evaluated using the listed values of $\phi_{(10\bar{1}0)}$ determined from the thin-slab calculation [33] (from Table II). It is noticeable that the values of Δp_T extracted from the DFT-based photoemission simulation are all significantly lower than Δp_{T0} . This is primarily due to the contribution of hole-like bands to photoemission for this hcp crystal orientation; unlike electron-like bands, hole-like states below the Fermi level are generally at higher p_T which reduces the available excess energy and hence the transmission efficiency over the work function barrier.

TABLE III. Photoemission properties of (10 $\bar{1}$ 0)-face hcp metals at $\hbar\omega=4.75$ eV

	$\phi_{(10\bar{1}0)}$ (eV)	$\Delta p_{T,(0001)}$ ($m_0\text{eV})^{1/2}$	$\Delta p_{T,(01\bar{1}0)}$ ($m_0\text{eV})^{1/2}$	Δp_{T0} ($m_0\text{eV})^{1/2}$
Be	$3.88(\pm 0.05)$	$0.147(\pm 0.005)$	$0.312(\pm 0.010)$	$0.54(\pm 0.02)$
Mg	$3.79(\pm 0.05)$	$0.221(\pm 0.006)$	$0.313(\pm 0.008)$	$0.57(\pm 0.02)$
Y	$3.08(\pm 0.05)$	$0.285(\pm 0.004)$	$0.316(\pm 0.005)$	$0.76(\pm 0.02)$
Zr	$3.59(\pm 0.05)$	$0.309(\pm 0.007)$	$0.325(\pm 0.007)$	$0.62(\pm 0.02)$

Figure 2(c) (right panel) displays the photon energy dependence of both $\Delta p_{T,(0001)}$ and $\Delta p_{T,(01\bar{1}0)}$ determined by the DFT-based analysis for (10 $\bar{1}$ 0)-face emission from the four hcp crystalline photocathodes. In all cases, the theoretical data points are well fit by $\Delta p_T = A\sqrt{(m_0\Delta E)}$ (solid lines). The ratios of the extracted values of A are again consistent with the anisotropy trends associated with the photoemitting states (Fig. 2(b)); namely, $A_{(01\bar{1}0)} = 2.10A_{(0001)} = 0.336$ for Be(10 $\bar{1}$ 0), $A_{(01\bar{1}0)} = 1.33A_{(0001)} = 0.320$ for Mg(10 $\bar{1}$ 0),

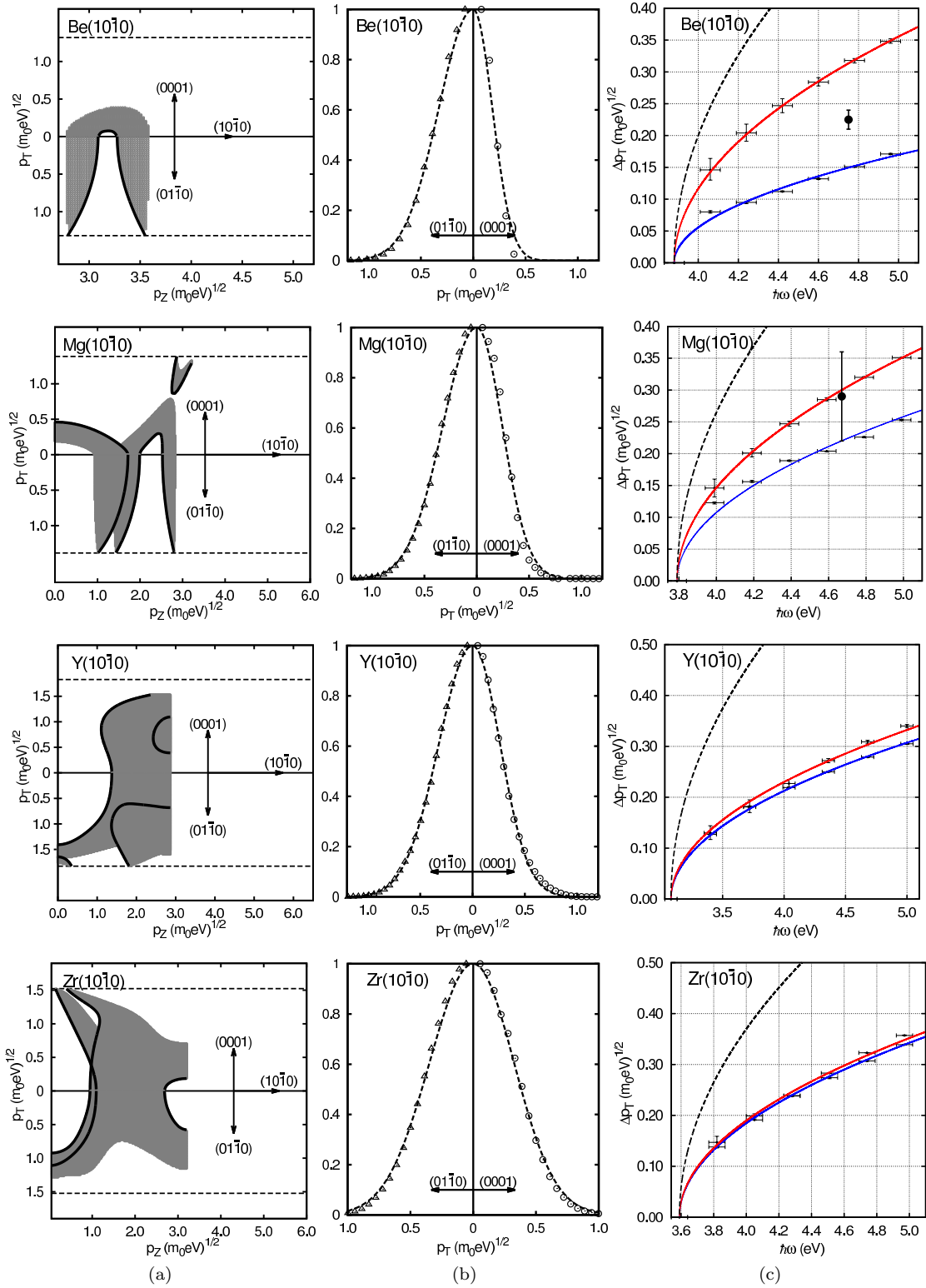


FIG. 2. Emission properties for $(10\bar{1}0)$ face of Be, Mg, Y and Zr metals. Column (a): Crystal momentum map of the electronic states (shaded regions) below the Fermi level (solid line) that may photoemit within $p_{T,max.} = \sqrt{2m_0\Delta E}$ (dashed lines) for the transverse (0001) and $(01\bar{1}0)$ crystal directions. Column (b): Transverse momentum distributions of the photoemitted electrons in the (0001) and $(01\bar{1}0)$ directions (Gaussian fits are guides to the eye). Column (c): Incident photon energy dependence of the rms transverse momentum Δp_T for electron temperatures $T_e \rightarrow 0$ (data points with solid red line fit, for $(01\bar{1}0)$ crystal direction and solid blue line fit for (0001) crystal direction), together with the expected form of $\Delta p_T(\hbar\omega)$ from Refs. [14] and [15] (dashed line). Black circles show the experimental measured Δp_T data from Refs. [34] and [35] for Be and Mg, respectively.

$A_{(01\bar{1}0)} = 1.08A_{(0001)} = 0.240$ for $Y(10\bar{1}0)$, and $A_{(01\bar{1}0)} = 1.03A_{(0001)} = 0.296$ for $Zr(10\bar{1}0)$. Further, in all four

cases, the values of the rms transverse momentum extracted from the DFT-based analysis is on average a factor of 2 lower than $\Delta p_{T0}(\hbar\omega)$, which is shown by the dashed line in the right panel of Fig. 2. This is, however, consistent with the available experimental data for polycrystalline Be [34] and Mg [35] photocathodes, which are expected to preferentially expose $(10\bar{1}0)$ microcrystalline faces [72]. For Mg with $\hbar\omega = 4.66\text{eV}$, Wang et al. [35] report an upper limit on the normalized transverse emittance of $0.40(\pm 0.1)\text{ mm.mrad/mm}$, which equates to $\Delta p_T = 0.290(\pm 0.07) (m_0\text{eV})^{1/2}$ — a value that is plotted in Fig. 2(c) for Mg($10\bar{1}0$) emission, the error bars of the experimental Δp_T values for Mg come from Schottky effect caused effective work function uncertainty. Similarly, the span of the two directional transverse values of Δp_T predicted for Be($10\bar{1}0$) emission is consistent with the value of $0.225(\pm 0.015) (m_0\text{eV})^{1/2}$ (also plotted in Fig. 2(c)) determined for a polycrystalline Be photocathode using the solenoid scan technique with a 20kV DC photo-gun and 4.75 eV photons [34].

We also note that in accordance with the results for Mg(0001) emission (Section IV), the DFT-based photoemission analysis indicates that electron temperature T_e has little effect on Δp_T up to the melting points [71] of the four investigated hcp metal photocathodes. In particular, the values of A in $\Delta p_T = A\sqrt{m_0\Delta E}$ do not change by more than about 1%, which is well within the intrinsic uncertainty of the simulation technique. To a large extent, this temperature insensitivity is due to the preponderance of hole-like states for $(10\bar{1}0)$ -face emission, for which higher electron temperatures generate occupation in higher energy states with lower p_T that therefore do not contribute to significant increase in Δp_T .

VI. THE Be(0001) CRYSTAL FACE

Photoemission from the (0001) face of hcp metals generally produces a relatively isotropic rms transverse momentum distribution since the basal plane band dispersion is also quite isotropic, as shown for Mg(0001) in Fig. 1. This is also true for Be(0001) emission with the additional complication that for a clean surface there exists a strong two-dimensional surface state in the 6 eV energy gap between the Γ_3^+ and Γ_4^- bulk electronic bands with a near-perfect parabolic dispersion centered on the Γ point of the surface Brillouin zone [36, 37, 73–75]. Other hcp metals also possess a surface state (e.g., Mg(0001) [76, 77]), but the Fermi level usually cuts the upper Γ_4^- band ensuring that there are filled bulk states around the Γ point that contribute to and may dominate the photoemission from the (0001) face. For Be(0001), the situation is different: The upper Γ_4^- bulk band is not occupied and the surface state lies 1.8 eV above the lower Γ_3^+ bulk band at zone center and its $\bar{\Gamma}$ point is 2.8 eV below the Fermi level [36, 37]. Angle-resolved photoemission spectroscopy measurements [36] have indicated that the effective mass of the surface state is about $1.50m_0$;

$m^* = 1.53m_0$ in the $\bar{\Gamma} \rightarrow \bar{M}$ direction and $m^* = 1.45m_0$ in the $\bar{\Gamma} \rightarrow \bar{K}$ direction. This means that photoemission from the surface state of Be(0001) will first occur from states around the $\bar{\Gamma}$ point as this requires the least energy — an argument that is also true for emission from the lower Γ_3^+ bulk band since its effective mass is again greater than m_0 [78]. Consequently, our DFT-based analysis predicts that photoemission from the Be(0001) face only occurs for the surface state when $\hbar\omega > \phi_{(0001)} + 2.8\text{ eV}$ and for the bulk states when $\hbar\omega > \phi_{(0001)} + 4.6\text{ eV}$, where $\phi_{(0001)} = 5.61\text{ eV}$.

For the theoretical determination of the characteristics of the Be(0001) surface state within our DFT framework, thin-slab calculations employing the LDA pseudopotentials [39] in the Quantum-ESPRESSO code [38] are used. The surface is modeled in the two-dimensional irreducible surface Brillouin zone (SBZ) with 13 atomic layers separated by 15 Å of vacuum — the slab configuration used to obtain a reasonable value for the work function for the Be(0001) surface, which then sets the energy scale for the two-dimensional quantum-confined surface state. Figure 3 shows the results of the computed Be(0001) surface state electronic structure in the two transverse symmetry directions ($\bar{\Gamma}\bar{M}$ and $\bar{\Gamma}\bar{K}$) of the SBZ along with the projected bulk states. The calculated minimum energy of the surface state (solid red line) at the $\bar{\Gamma}$ point is 2.83 eV below the Fermi level (dashed line), which is in good agreement with the experimental value of $2.8(\pm 0.05)\text{ eV}$ [36, 37]. Further, our evaluation of the Be(0001) surface state indicates that the dispersion of the confined state is quite isotropic with a transverse effective mass $m_T^* \approx 1.5m_0$, in agreement with prior work [36]. At the $\bar{\Gamma}$ point, the surface state band calculated to be 1.92 eV above the minimum energy at the same crystal momentum of the lower bulk band Γ_3^+ from which the electrons in the surface state originate [36, 37, 79]. This ‘zero point’ energy ΔE_{ss} then allows evaluation of the longitudinal momentum of the electrons in the surface state; $p_z = \sqrt{2m_{ss}^*\Delta E_{ss}} \approx 2.4 (m_0\text{eV})^{1/2}$, if one assumes $m_{ss}^* \approx 1.5m_0$ is also the effective electron mass of the surface state in the z direction.

With these assumed constant values of p_z and m_z for the emitting state, all required parameters in our DFT photoemission analysis are defined; in particular, those associated with the flux transmission probability over the work function barrier (Equation (2)). The predicted p_T distribution of the emitted electrons for an excess energy $\Delta E = 0.3\text{ eV}$ (a photon energy $\hbar\omega = 8.74\text{ eV}$ (142 nm)) is shown in Figure 4. As $m_T^* > m_0$ and the surface state has a constant density of states $g(E, \vec{k})$, electrons are predominantly photoemitted from the $\bar{\Gamma}$ point and no electrons may be emitted beyond $p_{T,max}\sqrt{2m_0\Delta E} \approx 0.77 (m_0\text{eV})^{1/2}$. In practice, $T(p_z, p_{z0})$ severely curtails emission beyond $p_T = 0.5 (m_0\text{eV})^{1/2}$, resulting in a predicted value of $\Delta p_{T,\text{Be}(0001)} = 0.141(\pm 0.05) (m_0\text{eV})^{1/2}$. As expected from the isotropic dispersion of the two-dimensional surface state, the p_T distribution is also symmetric with respect to $p_T = 0$.

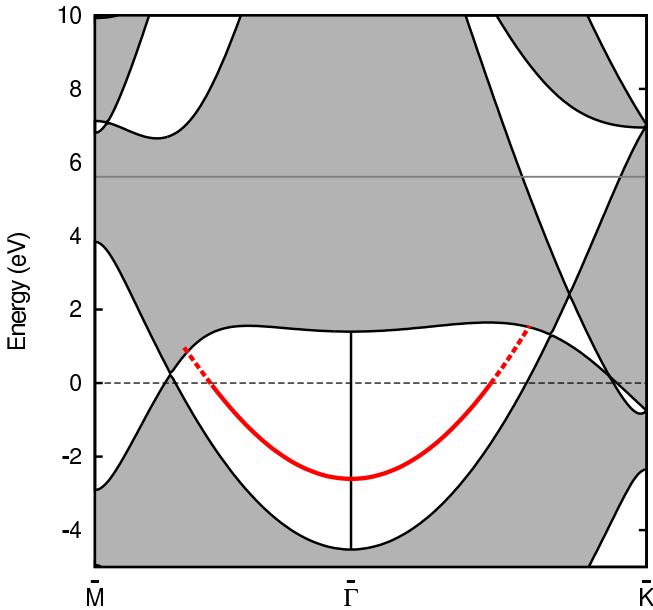


FIG. 3. Be(0001) bulk and surface state band results. The projected bulk states are in gray and the red solid line is Be(0001) surface state under Fermi level whereas the red dashed line is Be(0001) surface state above Fermi level. The DFT evaluated vacuum level at 5.61 eV is indicated by a thin solid line.

VII. SUMMARY

The presented DFT-based analysis of the properties of photocathodes clearly indicates that the rms transverse momentum Δp_T of electrons photoemitted in a one-step quantum mechanical process [80, 81] is fundamentally dependent upon the dispersive nature of the electronic bands from which they originate. This is shown to be particularly true of the hcp metals — the most common crystal structure amongst the elemental metals — since the crystal symmetry, and hence electronic band structure, is intrinsically anisotropic. Whereas emission from the basal plane, the (0001)-face, usually generates an isotropic transverse momentum distribution (Fig. 1) due to hexagonal face symmetry, emission from the generally most prevalent (1010)-face in polycrystalline hcp metals can be quite anisotropic (Fig. 2). As the rms transverse momentum Δp_T is also dependent on the excess photoemission energy, knowledge of the work function for each crystal emission face, ϕ_{ijkl} , is also critical to the DFT-based photoemission simulation. A standard thin-slab evaluation method for ϕ [33], that employs the atomic crystal potential from the band structure calculations, is shown to provide values in good agreement with literature values. The average of the resulting anisotropic values of Δp_T obtained from the theoretical simulation for the most prevalent (1010)-face of Be and Mg are consistent with experimental measurements [46, 70, 82–86].

Emission from the strong surface state of the Be(0001) face [36, 37, 75] is also analyzed. As the effective mass

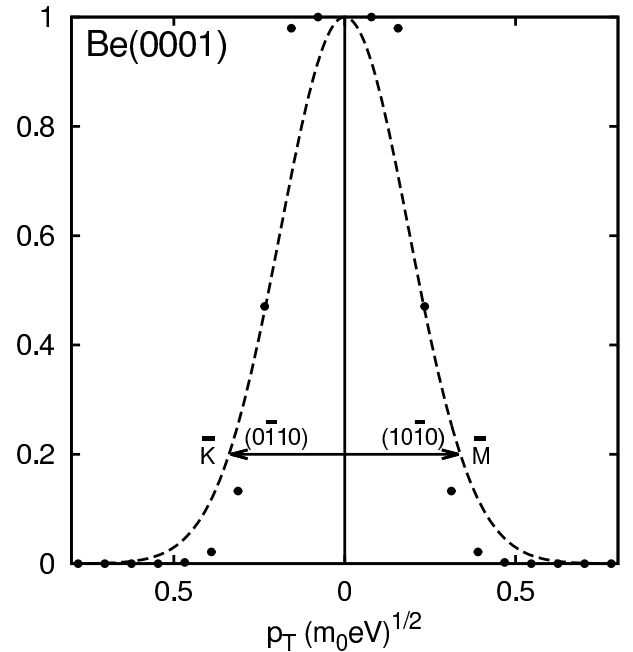


FIG. 4. Be(0001) photoemission result for surface state. Solid dots stand for calculated momentum distribution on the surface Brillouin zone. Transverse momentum distributions of the photoemitted electrons in the \bar{M} and \bar{K} directions whereas the $(10\bar{1}0)$ and $(01\bar{1}0)$ directions in bulk state (Gaussian fit is guide to the eye (dashed line)).

m^* associated with the dispersion of this two-dimensional state is greater than m_0 and fairly symmetric, the transverse momentum distribution of the photoemitted electrons is maximized at and quite symmetric about $p_T = 0$ (the $\bar{\Gamma}$ point of the surface Brillouin zone). If its effective mass were less than m_0 , the one-step analysis would predict emission peaked at $p_T = \sqrt{2m^*E_F}$, which may then directly produce an electron beam suitable for hollow cone illumination [87–89]. The use of such a state can be dependent upon the cleanliness of the laser-driven electron gun since chemical contamination of the photocathode surface may destroy environmentally sensitive surface states. Similar considerations also affect the use of bulk elemental hcp metal photocathodes and together with impractical high work functions, low melting points, and magnetic effects effectively restrict the choice to only a handful of elemental hcp metals: Be, Mg, Y, and Zr. Bi-metal hcp compounds may well overcome many such issues.

ACKNOWLEDGMENTS

The authors are indebted to Juan Carlos Campuzano, Christopher Grein, Randall Meyer, and Serdar Oğüt for their valuable discussions. This work was partially supported by the Department of Energy (Contract No. DE-FG52-09NA29451).

- [1] Z. Huang and K.-J. Kim, Phys. Rev. ST Accel. Beams **10**, 034801 (2007).
- [2] K. Németh, K. C. Harkay, M. van Veenendaal, L. Spentzouris, M. White, K. Attenkofer, and G. Srajer, Phys. Rev. Lett. **104**, 046801 (2010).
- [3] V. A. Lobastov, R. Srinivasan, and A. H. Zewail, Proc. Natl. Acad. Sci. USA **102**, 7069 (2005).
- [4] M. R. Armstrong, B. W. Reed, B. R. Torralva, and N. D. Browning, Applied Physics Letters **90**, 114101 (2007), <http://dx.doi.org/10.1063/1.2712838>.
- [5] O. Bostanjoglo and R. Liedtke, Phys. Status Solidi A **60**, 451 (1980).
- [6] H. Dmer and O. Bostanjoglo, Rev. Sci. Instrum. **74** (2003).
- [7] M. Reiser, *Theory and design of charged particle beams* (John Wiley & Sons, 2008).
- [8] C. D. Child, Phys. Rev. (Series I) **32**, 492 (1911).
- [9] I. Langmuir, Phys. Rev. **21**, 419 (1923).
- [10] T. Srinivasan-Rao, J. Fischer, and T. Tsang, J. Appl. Phys. **69**, 3291 (1991).
- [11] T. Anderson, I. V. Tomov, and P. Rentzepis, J. Appl. Phys. **71**, 5161 (1992).
- [12] A. Valfells, D. W. Feldman, M. Virgo, P. G. O'Shea, and Y. Y. Lau, Phys. Plasmas **9**, 2377 (2002).
- [13] I. V. Bazarov, B. M. Dunham, and C. K. Sinclair, Phys. Rev. Lett. **102**, 104801 (2009).
- [14] D. H. Dowell and J. F. Schmerge, Phys. Rev. ST Accel. Beams **12**, 074201 (2009).
- [15] K. L. Jensen, P. G. O'Shea, D. W. Feldman, and J. L. Shaw, Journal of Applied Physics **107**, 014903 (2010), <http://dx.doi.org/10.1063/1.3267288>.
- [16] J. Simmons, Phys. Rev. Lett. **15**, 967 (1965).
- [17] R. W. Stark and L. M. Falicov, Phys. Rev. Lett. **19**, 795 (1967).
- [18] V. Fomenko, Powder Metall. Met. Ceram. **33**, 85 (1995).
- [19] M. Methfessel, D. Hennig, and M. Scheffler, Phys. Rev. B **46**, 4816 (1992).
- [20] Y. Morikawa, H. Ishii, and K. Seki, Phys. Rev. B **69**, 041403 (2004).
- [21] N. D. Lang and W. Kohn, Phys. Rev. B **3**, 1215 (1971).
- [22] R. Klein, Surf. Sci. **20**, 1 (1970).
- [23] V. Sahni, J. P. Perdew, and J. Gruenebaum, Phys. Rev. B **23**, 6512 (1981).
- [24] H. L. Skriver and N. M. Rosengaard, Phys. Rev. B **46**, 7157 (1992).
- [25] R. C. Jerner and C. B. Magee, Oxid. Met **2**, 1 (1970).
- [26] R. G. Wilson, J. Appl. Phys. **37**, 2261 (1966).
- [27] A. K. Green and E. Bauer, Surf. Sci. **74**, 676 (1978).
- [28] F. Batallan, I. Rosenman, and C. B. Sommers, Phys. Rev. B **11**, 545 (1975).
- [29] Y. Ishizawa and W. R. Datars, Phys. Rev. B **2**, 3875 (1970).
- [30] P. Chatterjee, Phys. Rev. B **27**, 4722 (1983).
- [31] N. Lang and W. Kohn, Phys. Rev. B **3**, 1215 (1971).
- [32] H. L. Skriver and N. M. Rosengaard, Phys. Rev. B **46**, 7157 (1992).
- [33] C. J. Fall, N. Binggeli, and A. Baldereschi, J. Phys. Condens. Matter **11**, 2689 (1999).
- [34] B. L. Rickman, J. A. Berger, A. W. Nicholls, and W. A. Schroeder, Phys. Rev. Lett. **111**, 237401 (2013); **113**, 239904 (2014), [erratum].
- [35] X. J. Wang, M. Babzien, R. Malone, and Z. Wu, in *Proc. EPAC* (2000).
- [36] J. C. Boettger and S. B. Trickey, Phys. Rev. B **34**, 3604 (1986).
- [37] R. A. Bartynski, E. Jensen, T. Gustafsson, and E. W. Plummer, Phys. Rev. B **32**, 1921 (1985).
- [38] P. G. et al., J. Phys. Condens. Matter **21**, 395502 (19pp) (2009).
- [39] K. F. Garrity, J. W. Bennett, K. M. Rabe, and D. Vanderbilt, Comput. Mater. Sci. **81**, 446 (2014).
- [40] J. P. Perdew, K. Burke, and M. Ernzerhof, Phys. Rev. Lett. **77**, 3865 (1996).
- [41] H. J. Monkhorst and J. D. Pack, Phys. Rev. B **13**, 5188 (1976).
- [42] N. Marzari, D. Vanderbilt, A. De Vita, and M. Payne, Phys. Rev. Lett. **82**, 3296 (1999).
- [43] O. Jepsen, O. K. Andersen, and A. R. Mackintosh, Phys. Rev. B **12**, 3084 (1975).
- [44] P. Soven, Phys. Rev. **137**, A1706 (1965).
- [45] C. M. Singal and T. P. Das, Phys. Rev. B **16**, 5068 (1977).
- [46] T. L. Loucks and P. H. Cutler, Phys. Rev. **133**, A819 (1964).
- [47] H. Gotsis, D. Papaconstantopoulos, and M. Mehl, Phys. Rev. B **65**, 134101 (2002).
- [48] L. F. Mattheiss, Phys. Rev. **151**, 450 (1966).
- [49] S. L. Altmann and C. J. Bradley, Proc. Phys. Soc. **92**, 764 (1967).
- [50] C. Kittel and P. McEuen, *Introduction to solid state physics*, Vol. 8 (Wiley New York, 1976).
- [51] P. M. Holtham, J.-P. Jan, and H. L. Skriver, J. Phys. F **7**, 635 (1977).
- [52] R. A. Deegan, Phys. Rev. **171**, 659 (1968).
- [53] D. G. Pettifor, J. Phys. F **7**, 613 (1977).
- [54] C. J. Fall, N. Binggeli, and A. Baldereschi, J. Phys. Condens. Matter **11**, 2689 (1999).
- [55] N. E. Singh-Miller and N. Marzari, Phys. Rev. B **80**, 235407 (2009).
- [56] M. Green, *Solid state surface science*, Vol. 1 (M. Dekker, 1969).
- [57] H. B. Michaelson, Journal of Applied Physics **48** (1977).
- [58] E. V. Chulkov, V. M. Silkin, and E. N. Shirykalov, Surf. Sci. **188**, 287 (1987).
- [59] P. O. N. Sobczak, E. and K. Karlsson., Acta Phys. Pol. SERIES A, 337 (1992).
- [60] J. Lahtinen, J. Vaari, and K. Kauraala, Surf. Sci. **418**, 502 (1998).
- [61] H. Kawano, Progress in Surface Science **83**, 1 (2008).
- [62] F. J. Himpsel, K. Christmann, P. Heimann, D. E. Eastman, and P. J. Feibelman, Surf. Sci. **115**, L159 (1982).
- [63] D. M. Hanson, R. Stockbauer, and T. E. Madey, Phys. Rev. B **24**, 5513 (1981).
- [64] M. Yamamoto, C. T. Chan, and K. M. Ho, Phys. Rev. B **50**, 7932 (1994).
- [65] S. Davis, J. Catal. **122**, 240 (1990).
- [66] G. W. Mahlman, J. Appl. Phys. **20**, 197 (1949).
- [67] J. A. Berger, B. L. Rickman, T. Li, A. W. Nicholls, and W. A. Schroeder, Appl. Phys. Lett. **101**, 194103 (2012).
- [68] J. Chen, D. Tzou, and J. Beraun, Int. J. Heat Mass Transfer **49**, 307 (2006).
- [69] E. Jeon, J. Kim, Y. Kim, K. Ma, and J. Nam, Nucl. Instrum. Methods Phys. Res., Sect. A **697**, 46 (2013).

- [70] J. C. Kimball, R. W. Stark, and F. M. Mueller, Phys. Rev. **162**, 600 (1967).
- [71] W. M. Haynes, *CRC handbook of chemistry and physics* (CRC press, 2013).
- [72] U. F. Kocks, C. N. Tomé, and H.-R. Wenk, *Texture and anisotropy: preferred orientations in polycrystals and their effect on materials properties* (2000).
- [73] P. J. Feibelman, Phys. Rev. B **46**, 2532 (1992).
- [74] K. Pohl, J.-H. Cho, K. Terakura, M. Scheffler, and E. W. Plummer, Phys. Rev. Lett. **80**, 2853 (1998).
- [75] P. T. Sprunger, L. Petersen, E. W. Plummer, E. Lægsgaardgsgaard, and F. Besenbacher, Science **275**, 1764 (1997).
- [76] E. Chulkov, V. Silkin, and E. Shiryalov, Surf. Sci. **188**, 287 (1987).
- [77] U. O. Karlsson, G. Hansson, P. Persson, and S. Flodström, Phys. Rev. B **26**, 1852 (1982).
- [78] J. H. Tripp, P. M. Everett, W. L. Gordon, and R. W. Stark, Phys. Rev. **180**, 669 (1969).
- [79] V. Silkin, T. Balasubramanian, E. Chulkov, A. Rubio, and P. Echenique, Physical Review B **64** (2001), 10.1103/PhysRevB.64.085334.
- [80] G. Mahan, Phys. Rev. B **2**, 4334 (1970).
- [81] R. Courths and S. Hüfner, Phys. Rep. **112**, 53 (1984).
- [82] B. Watts, Phys. Lett. **3**, 284 (1963).
- [83] A. Stewart, J. Shand, J. Donaghy, and J. Kusmiss, Phys. Rev. **128**, 118 (1962).
- [84] R. Stark, Phys. Rev. **162**, 589 (1967).
- [85] J. Ketterson and R. Stark, Phys. Rev. **156**, 748 (1967).
- [86] L. M. Falicov, Philos. Trans. R. Soc. London, Ser. A **255**, 55 (1962).
- [87] W. Krakow and L. A. Howland, Ultramicroscopy **2**, 53 (1976).
- [88] C. Dinges, H. Kohl, and H. Rose, Ultramicroscopy **55**, 91 (1994).
- [89] Y. Kondo, T. Ito, and Y. Harada, Jpn. J. Appl. Phys. **23**, L178 (1984).